Available online at www.sciencedirect.com
SCIENCE DIRECT®
Journal of Sound and Vibration 275 (2004) 89–106
JOURNAL OF SOUND AND VIBRATION
www.elsevier.com/locate/jsvi

Wave propagation in a weak viscoelastic layer produced by prescribed velocity on the boundary

M. El-Raheb*

1000 Oak Forest Lane, Pasadena, CA 91107, USA

Received 31 July 2002; accepted 18 June 2003

Abstract

Four models are employed to analyze wave propagation from impact on a weak viscoelastic layer. Each model is exploited on the basis of its particular strength and all four are used co-operatively in a study that overcomes the limitations of each. These models are: a numerical finite volume model serving as reference which couples motions of projectile and layer, a two-dimensional viscoelastic model with prescribed pressure on the boundary, and two versions of a three-dimensional axisymmetric elastic model; one with prescribed pressure at the boundary, and one with prescribed velocity at the boundary. This last model superimposes the responses from several external annular pressure segments of unit intensity with time-dependent weights yielding a combined response equal to the prescribed instantaneous velocity. Stress histories from all models are comparable with greatest difference near the excited boundary.

1. Introduction

Wave propagation in semi-infinite and finite elastic media has been treated extensively in the literature. Methods of solution include such discretizations as finite element, finite difference, finite volume, smooth particle hydrodynamics and boundary element methods [1–12], meshless methods [13], and such hybrid analytical/numerical methods as modal analysis and integral methods. A related but more challenging problem includes media with viscoelastic properties. One application is linear stress waves from low velocity impact in weak viscoelastic materials simulating blunt trauma in living tissue. The properties may be approximated by a polymeric gelatin that has an acoustic impedance close to that of water yet it dissipates energy from viscoelasticity and possesses shear rigidity controlling transverse propagation.

*Tel.: +1-626-796-5528; fax: +1-626-583-8834.
E-mail address: mertrident@earthlink.net (M. El-Raheb).

0022-460X/$ - see front matter
doi:10.1016/S0022-460X(03)00787-9

A substantial body of literature concerning lung and brain tissue trauma was published by the University of Pennsylvania Injury biomechanics Laboratory. One such model employs the ANSYS finite element program (ANSYS Inc., Houston, PA) with a heuristic time-dependent shear modulus independent of strain and its temporal derivatives: $G(t) = G_\infty + (G_o - G_\infty)e^{-\beta t}$. However, all these studies concern forcing pulses lasting over a millisecond where simple viscoelastic constitutive models may apply. In this work, the duration of the forcing pulse is of the order of a few microseconds where more refined viscoelastic constitutive models are valid.

Despite their ability to handle general geometries and material properties, relying on pure numerical methods alone has the following drawbacks:

(1) They require artificial viscosity to stabilize the numerical time integration which will mask the effects of material viscoelasticity.
(2) They fail to reproduce the rapid rise time predicted by even a one-dimensional (1-D) model which includes viscoelasticity.
(3) The type of viscosity that can be accounted for by the constitutive model is in terms of a convolution integral rather than the more general differential form determined by fitting experimental data in the frequency domain.

An analytical method will require as one of its input a realistic forcing function. This can be approximated with confidence by the velocities predicted by either the purely numerical model or a 1-D coupled viscoelastic model in those cases where these two predictions are in close agreement soon after impact. The type of analytical model closest to the application would include all three dimensions. However if a two-dimensional (2-D) analytical model could be constructed capable of predicting the same results, then this model will be preferred for parametric studies. The form of the forcing function closest to the application is a prescribed velocity at the boundary, yet this would lead to a mixed boundary condition. This difficulty can be overcome by constructing a corresponding 3-D axisymmetric model that superimposes responses from a set of unit pressures with time-dependent weights prescribed on annular portions of the boundary. These weights are updated at each time step from the condition that the combined velocity response at the footprint equals the prescribed instantaneous velocity. In this way, the forcing function is converted to pure traction with time varying spatial dependence. These considerations motivate a study that includes constructing and comparing four different models: a purely numerical coupled finite volume model; two 3-D axisymmetric analytical models, one with prescribed pressure and the other with prescribed velocity; and a 2-D analytical model useful for a parametric study.

A finite volume model (Model 1) developed in Ref. [14] is employed to calculate the coupled response. The average pressure over the footprint is applied as a forcing function to an elastic 3-D axisymmetric analytical model (Model 2A) developed in Ref. [15]. The same forcing function is also applied to a 2-D model (Model 3) developed in Ref. [16], including a viscoelastic constitutive law. Comparison of results from the 3-D and 2-D models demonstrates the sensitivity of the response to problem dimensionality.

The finite volume model of impact [14] reveals that velocity at the footprint is nearly constant throughout the duration of impact. The 1-D model coupling projectile and disk when their radii extend to infinity replicates this result. This motivates the 3-D axisymmetric Model 2B [15] with prescribed velocity at the boundary that does not rely on the input from the finite volume model.

Section 2 compares histories from the finite volume Model 1, the 3-D axisymmetric Model 2A and the 2-D Model 3. Section 3 discusses the influence method behind Model 2B to include a prescribed velocity at the footprint. The coupled 1-D model including viscoelasticity is developed to compute peak pressure and velocity history at the footprint. Section 4 discusses effects of damping on 1-D stress and velocity histories. Histories from Model 2B are then compared to those from the other models with emphasis on stress history and its radial distribution over the footprint.

2. Comparison of histories from Models 1, 2A and 3

In all results to follow, geometric and material properties of plastic cylindrical projectile and gelatin disk are listed in Table 1, where E is the elastic modulus, ρ is mass density, v is Poisson ratio, h is axial length or thickness, r is radius, (c_d, c_s) are sound speeds of dilatational and shear waves, and ρc_d is acoustic impedance of dilatational waves. Except for c, subscripts "p" and "d" are used throughout the text to denote projectile and disk respectively. In Model 1, the projectile initial velocity is 20 m/s or 787 in/s. Also, all boundaries of the disk are stress free except at the projectile footprint. In Models 2A and 3, the disk is simply supported along its perimeter. For times soon after impact before reflections from the disk perimeter, the response is insensitive to boundary condition.

Figs. 1(a–c) illustrate instantaneous deformed shapes (snap-shots) of projectile and disk from Model 1. Since the projectile is an order of magnitude stiffer than the disk, the interface remains flat during the 15 μs event. At $t = 4$ μs, the wave front is almost planar consistent with 1-D propagation (see Fig. 1(a)). It evolves to a spherical front as it reaches the bottom boundary of the disk at $t = 8$ μs and reflects back toward the surface (see Fig. 1(b)). After the first reflection, a transverse wave front forms and propagates toward the disk perimeter (see Fig. 1(c)). Figs. 1(d–f) show the corresponding snap-shots from Model 2A. The top short vertical dashed lines symmetric about the disk axis mark the perimeter of the footprint. Unlike Model 1, the footprint in Model 2A is not flat, while it departs further from flatness as r increases. Also, bulging of material near the perimeter in Model 1 is more pronounced than in Model 2A because of the larger displaced volume in the former.

Table 1
Properties of projectile and gelatin layer

Property	Projectile	Gelatin
E (lb/in^2)	1.3×10^6	4.5×10^4
ρ (lb s^2/in^4)	9.3×10^{-5}	8.7×10^{-5}
υ	0.3	0.48
h (in)	0.98	0.49
r (in)	0.276	1.0
c_d (in/s)	1.372×10^5	6.74×10^4
c_s (in/s)	7.332×10^4	1.322×10^4
ρc_d (lb s/in^3)	12.76	5.86

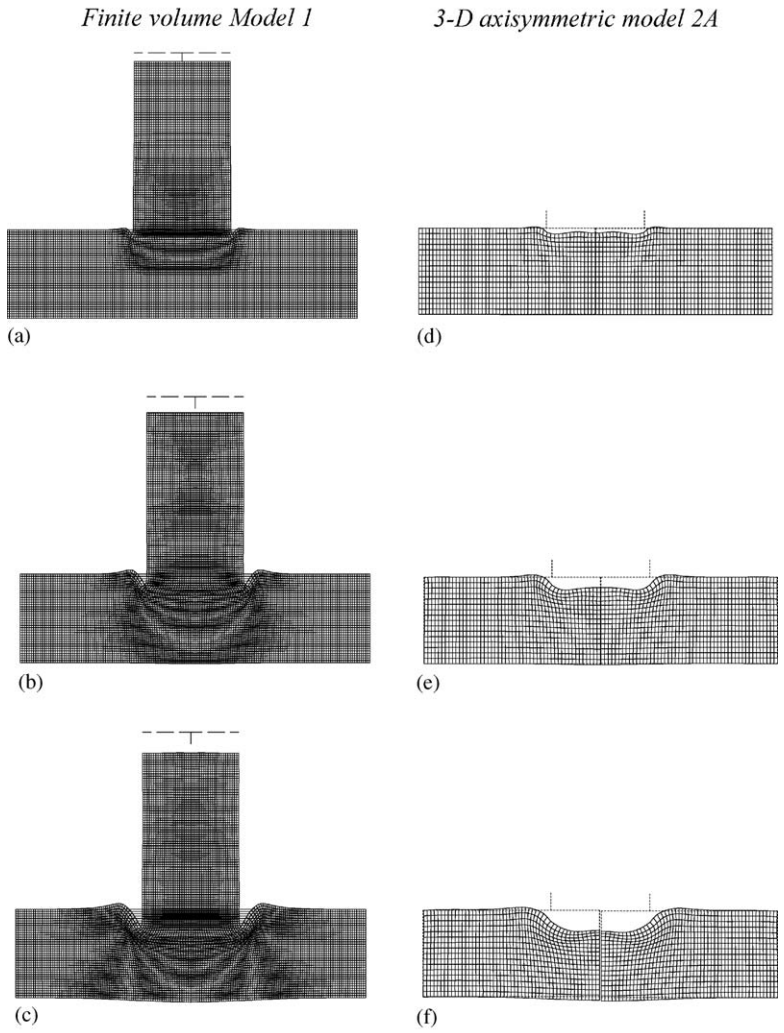

Fig. 1. Snap-shots from finite volume Model 1 (a)–(c) and 3-D axisymmetric Model 2A (d)–(f): (a), (d) $t = 4$ μs, (b), (e) $t = 8$ μs, (c),(f) $t = 12$ μs.

Fig. 2(a) plots average pressure p_{av} over the footprint from Model 1. The oscillations modulating the mean line are an artifact of the numerical analysis caused by reflections within a finite volume cell. This is shown by Table 2, where the period of oscillation is listed for three different choices of cell size, where the Δr is cell size, $\bar{\Omega}$ and $\bar{\tau}$ are frequency and period of oscillation, and $\bar{c}_r$ is a speed of propagation based on length scale $2\Delta r$ and time scale $\bar{\tau}$. The fact that $\bar{c}_r$ is almost constant for all cell sizes is consistent with the cause of these oscillations being numerical. Fig. 2(b) plots p_{av} smoothed by filtering the numerical oscillations. This smoothing, which can also be achieved by artificial viscosity, masks real viscous effects. Soon after impact, p_{av} attains its peak of 3×10^3 psi which is close to the 1-D result:

$$p_{1\text{-}D} = (\rho c)_{eq.} V_o = 3.16 \times 10^3 \text{ psi}, \tag{1}$$

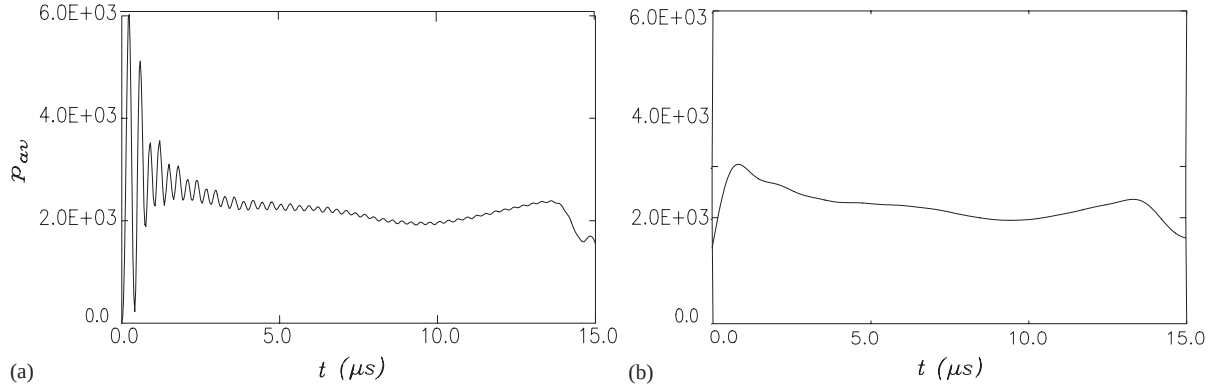

Fig. 2. History of average pressure over foot-print from finite volume Model 1: (a) original history, (b) smoothed history.

Table 2
Relationship between period of numerical oscillation and cell width

Δr (in)	$\bar{\Omega}$ (cyc./μs)	$\bar{\tau}$ (μs/cyc.)	$\bar{c}_r = 2\Delta r/\bar{\tau}$ (in/s)
0.0125	3.42	0.2924	8.55×10^4
0.0184	2.33	0.4292	8.57×10^4
0.0276	1.55	0.6452	8.56×10^4

where $1/(\rho c)_{eq.} = 1/(\rho c)_p + 1/(\rho c)_d$, and V_o is the initial velocity of projectile. p_{av} then diminishes with time because of the conversion of part of the axial momentum to radial momentum. The pulse width of 15 μs matches double the travel time along the projectile length. This also happens to coincide with double the travel time along the disk thickness.

Fig. 3 compares histories of axial displacement w, and radial and axial stress σ_{rr}, σ_{zz} from Model 1, and Model 2A excited by the uniformly distributed pressure pulse following p_{av} in Fig. 2(b). Sensors in the disk are close to impact at $z/h_d = 0.06$ and at three other radial stations. Fig. 3(a) plots the w history from Model 1. At all radial stations, the history is linear with slope equal to footprint velocity $V_{ft} \simeq 550$ in/s (14 m/s). This value is predicted from conservation of linear momentum in a 1-D model:

$$V_{ft} \simeq (\rho h)_p V_o/((\rho h)_p + (\rho h)_d) = 536.5 \text{ in/s } (\equiv 13.6 \text{ m/s}). \tag{2}$$

Fig. 3(d) plots w from Model 2A. There, the history deviates from linearity and the magnitude is smaller than that from Model 1 by 25%. Comparing histories of σ_{rr} from the two models (Figs. 3(b) and (e)) reveals that shapes are comparable and the magnitude from Model 2A is lower than that from Model 1 by 15% at $r/r_p = 0$. This difference drops to 5% at the other sensors. A similar observation applies to the σ_{zz} histories in Figs. 3(c) and (f). Fig. 4 compares histories of the two models at $z/h_d = 0.5$. At this depth, histories become closer in shape but differ in magnitude by 25% at $r/r_p = 0$. This difference diminishes when $r/r_p > 1$.

Fig. 5 plots histories from Model 3 at $z/h_d = 0.06$. Comparing Figs. 5(a–c) from Model 3 to Figs. 3(d–f) from Model 2A shows that histories from the two models are similar in shape and

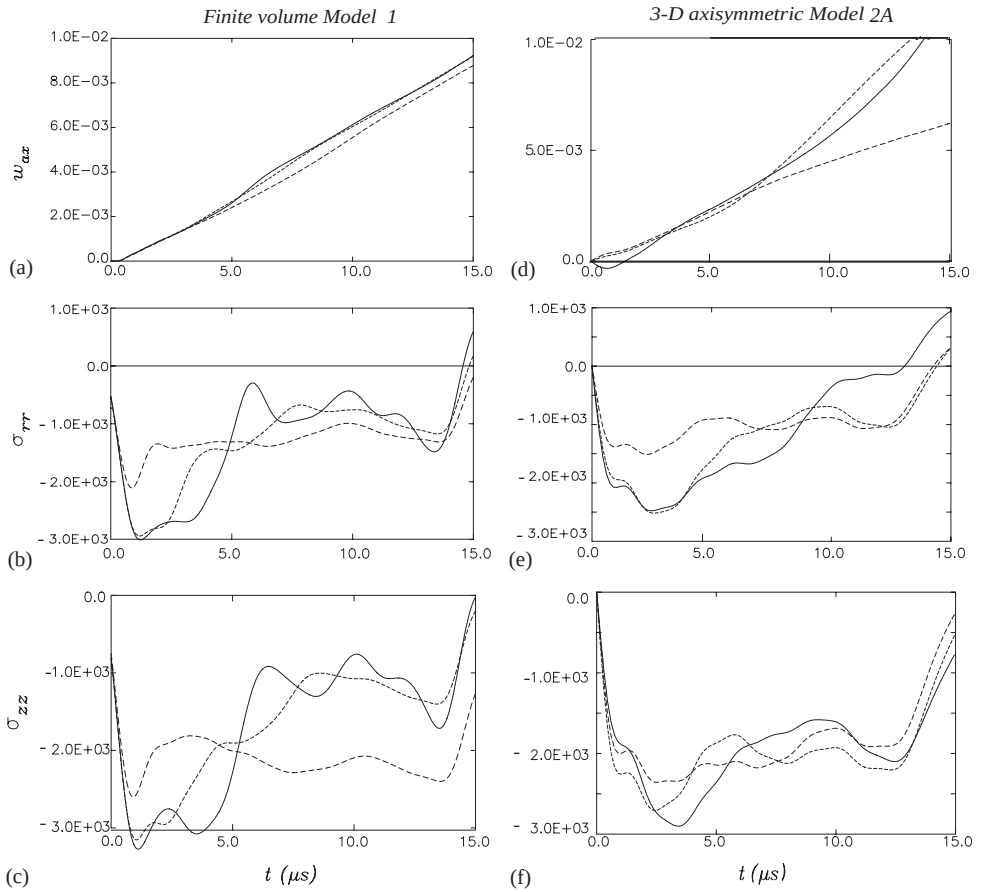

Fig. 3. Comparison of histories from finite volume Model 1: (a)–(c); and 3-D axisymmetric Model 2A with pressure excitation: (d)–(f); at $z/h = 0.06$; —— $r/r_p = 0$; - - - - -, $r/r_p = 0.5$; – – –, $r/r_p = 1$.

magnitude. This suggests that in this regime of velocities and material properties, the response is independent of dimensionality.

3. Model 2B with prescribed velocity

Close to impact, the main difference between Model 1 and Models 2A and 3 is the type of forcing function. The coupling in Model 1 is inherently a prescribed velocity while Models 2A and 3 are forced by prescribed pressure. The fact that in Model 1, velocity at the footprint is uniform along r and almost constant with time motivates Model 2B. The requirement of uniform velocity over the footprint is achieved as follows.

Divide the circle bounding the footprint into $n+1$ equidistant radial stations with increment Δr_p:

$$0, r_1, r_2, \ldots, r_{n-1}, r_p, \quad r_k - r_{k-1} = \Delta r_p = \text{const.} \tag{3}$$

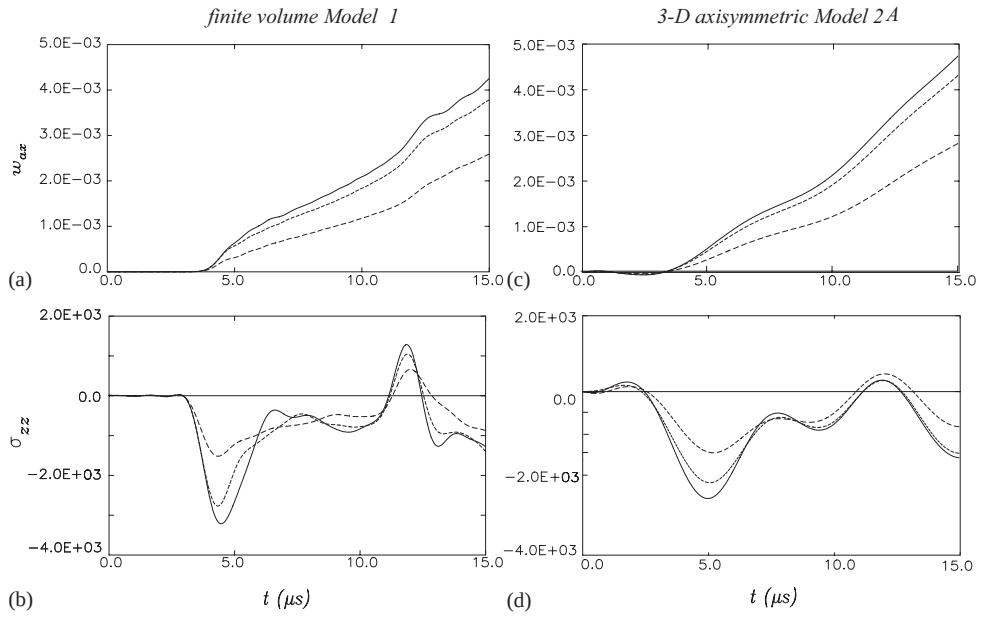

Fig. 4. Comparison of histories from finite volume Model 1: (a), (b); and 3-D axisymmetric Model 2A with pressure excitation: (c), (d); at $z/h = 0.5$; ——, $r/r_p = 0$; - - - - - , $r/r_p = 0.5$; – – –, $r/r_p = 1$.

Assume a uniform pressure of unit intensity to act over each annular segment $r_{k-1} \rightarrow r_k$. The elasto-dynamic solution to the k_{th} annular pressure segment is outlined below.

Expand each dependent variable in terms of eigenfunctions which satisfy homogeneous boundary conditions. Express the total displacement $\mathbf{u}_k(r, z; t)$ as a superposition of two terms,

$$\mathbf{u}_k(r, z; t) = \mathbf{u}_{sk}(r, z) f_p(t) + \mathbf{u}_D(r, z; t), \tag{4}$$

where $\mathbf{u}_{sk}(r, z)$ is the static displacement vector, $f_p(t)$ is the time dependence of the forcing pressure, and $\mathbf{u}_D(r, z; t)$ is a displacement vector satisfying the homogeneous dynamic equation of motion. Express $\mathbf{u}_D(r, z; t)$ in terms of the eigenfunctions $\mathbf{\Phi}_j(r, z)$,

$$\mathbf{u}_D(r, z; t) = \sum_j a_{jk}(t) \mathbf{\Phi}_j(r, z), \tag{5}$$

where $a_{jk}(t)$ is a generalized co-ordinate. Substituting Eqs. (4) and (5) in the dynamic equations of motion and enforcing orthogonality of $\mathbf{\Phi}_j(r, z)$ yields uncoupled equations in $a_{jk}(t)$. For an undamped elastic disk the equation governing $a_{jk}(t)$ is

$$\left(\frac{\mathrm{d}^2}{\mathrm{d}t^2} + \omega_j^2\right) a_{jk}(t) = \bar{f}_{jk}(t), \quad \bar{f}_{jk}(t) = N_{ajk} f_p(t)/N_j,$$

$$N_j = \int_0^{r_d} \int_0^h \mathbf{\Phi}_j^2(r, z)\, \mathrm{d}z\, r\, \mathrm{d}r, \quad N_{ajk} = \int_0^{r_d} \int_0^h \mathbf{u}_{sk}(r, z) \cdot \mathbf{\Phi}_j(r, z)\, \mathrm{d}z\, r\, \mathrm{d}r, \tag{6}$$

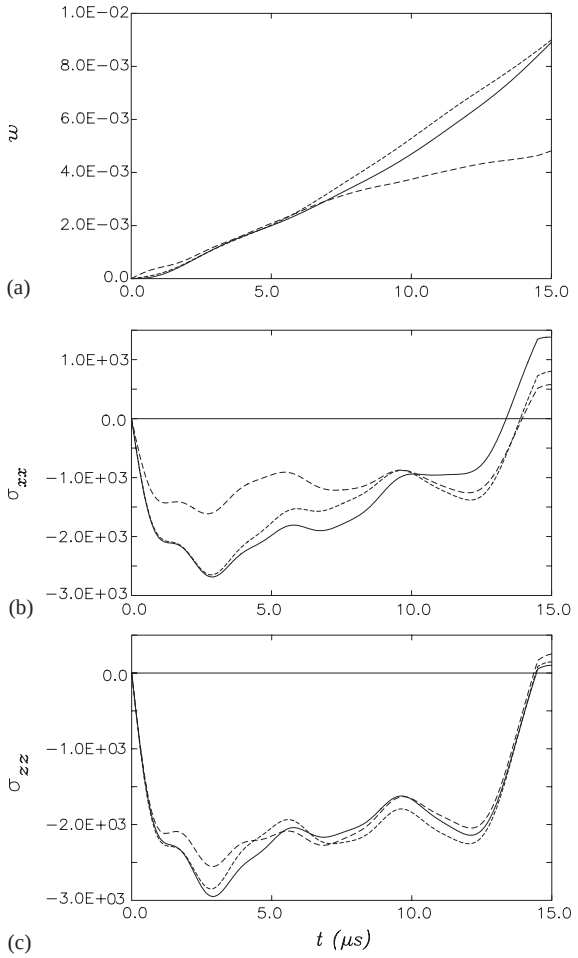

Fig. 5. Histories from 2-D Model 3 with pressure excitation at $z/h = 0.06$; ——, $r/r_p = 0$; - - - - -, $r/r_p = 0.5$; – – –, $r/r_p = 1$.

where ω_j is the resonant frequency in rad/s. The solution to Eq. (6) has the form

$$a_{jk}(t) = -\frac{1}{\omega_j}\int_0^t \sin\omega_j(t-\tau)\bar{f}_{jk}(\tau)\,\mathrm{d}\tau. \tag{7}$$

Evaluating axial displacement $w_k(r,z;t)$ from the kth pressure segment at each central point of a pressure segment $r_{cm} = (r_m + r_{m-1})/2$ yields the influence matrix

$$W_{km}(t) = \sum_j a_{jk}(t)\bar{w}_{jk}(r_{cm},0) + w_{sk}(r_{cm},0)f_p(t), \tag{8}$$

where $\bar{w}_{jk}(r_{cm},0)$ and $w_{sk}(r_{cm},0)$ are modal and static axial displacement at r_{cm} from the kth pressure segment. $f_p(t)$ in Eqs. (6) and (8) is a first approximation to the time dependence of

applied pressure. Enforcing the condition of prescribed displacement $w_p(t)$ at each time step yields a set of simultaneous equations in the weights $p_k(t)$:

$$\sum_{k=1}^{n} W_{mk}(t)p_k(t) = w_p(t), \quad m = 1, n. \tag{9}$$

The functions $f_p(t)$ and $w_p(t)$ are determined by solving the 1-D coupled problem of projectile and disk when their radii extend to infinity. A detailed derivation of this model including a viscoelastic constitutive law is presented in Appendix A.

4. Results

The 1-D Model is applied to the geometry and properties listed in Table 1 in the limit when radius of projectile and disk approaches infinity. A linear viscoelastic constitutive law is used for the gelatin disk in the form (see Appendix A, Eq. (A.17))

$$\sigma = E_{od}\frac{(1 + \tau_\sigma \mathrm{i}\omega)}{(1 + \tau_\varepsilon \mathrm{i}\omega)}\varepsilon, \tag{10}$$

where (σ, ε) are stress and strain and E_{od} is the rubbery modulus of the disk. The time constant τ_σ is assumed in the range $0 \leqslant \tau_\sigma \leqslant 5 \times 10^{-7}$ s with $\tau_\sigma/\tau_\varepsilon = 10$. The constant ratio of $\tau_\sigma/\tau_\varepsilon$ keeps rubbery modulus, glassy modulus and maximum loss coefficient constant for all τ_σ. Varying τ_σ shifts curves of $\log|E_c|$ and η along the $\log(\Omega)$ axis as shown in Figs. 6(a,b), where Ω is frequency in hertz.

Fig. 7 plots histories of stress σ_{zz} and velocity v from the 1-D Model at three stations across the thickness: $z/h = 0$, 0.5 and 1, where $z = 0$ is at the struck surface. The time for σ_{zz} to reach its peak is termed "rise time". Figs. 7(a) and (e) plot the undamped histories ($\tau_\sigma = 0$). Immediately after impact, σ_{zz} rises instantaneously to 3.16×10^3 psi as predicted by Eq. (1), and v rises to 13.6 m/s as predicted by Eq. (2). v is constant throughout the duration of impact. For $\tau_\sigma = 10^{-8}$ s, the rise time is 0.5 μs (see Fig. 7(b)), and v follows the same constant value as in the undamped case (see Fig. 7(f)). For $\tau_\sigma = 10^{-7}$ s, the rise time is 1 μs and the σ_{zz} plateau is modulated by a periodic oscillation. The response at $z/h = 0.5$ is smoother than that at $z/h = 0$ (see Fig. 7(c)). This also applies to v as shown in Fig. 7(g). There, the σ_{zz} plateau is higher than that in Fig. 7(b) because the transition frequency of the material falls within the frequency spectrum of the layer (see Fig. 6(a)). For $\tau_\sigma = 5 \times 10^{-7}$ s, the rise time reaches 2 μs, the plateau increases to 9×10^3 psi and its period of oscillation increases (see Fig. 7(d)). v at $z/h = 0$ is still constant at the undamped level (see Fig. 7(h)). The oscillations modulating the σ_{zz} plateau can be explained as follows. In the undamped case, the number of modes needed for convergence is infinite. As τ_σ increases, dissipation limits the contribution of the high frequency modes. This in turn reduces the initial slope of the σ_{zz} history which increases rise time and period of plateau oscillations.

In summary, viscoelasticity affects the 1-D response as follows:

(1) It increases rise time and period of plateau oscillations. The plateau increases with τ_σ because the transition frequency shifts and falls within the layer's frequency spectrum.
(2) Velocity is constant throughout impact and insensitive to τ_σ.

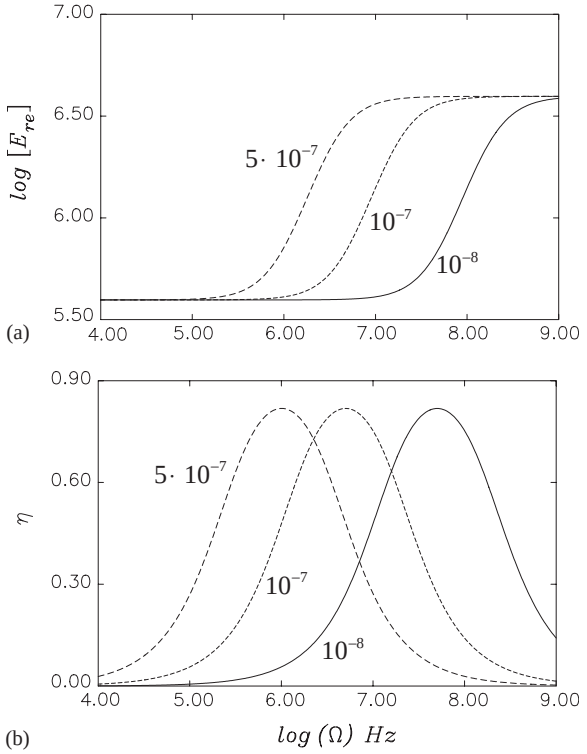

Fig. 6. Frequency-dependent visco-elastic properties for three τ_σ: (a) $\log[E_{re}]$, (b) η.

Fig. 8 plots histories from Model 2B using the integrated velocity from Fig. 7(g) for prescribed displacement $w_p(t) \simeq vt$, and the σ_{zz} history from Fig. 7(c) as a first approximation to $f_p(t)$. Histories of w, σ_{rr} and σ_{zz} from Model 2B in Figs. 8(a–c) agree closely in shape and magnitude to those from Model 1 in Figs. 3(a–c). This shows that response close to impact is sensitive to the spatial distribution of applied pressure. It also demonstrates that prescribing velocity instead of pressure more closely approximates the coupled problem of projectile and disk in Model 1 provided the disk material is sufficiently weaker than projectile material.

Fig. 9 illustrates snap-shots of the disk using Model 2B. These resemble the snap-shots in Fig. 1 from Model 1 in flatness over the footprint and bulging of material near the perimeter.

Fig. 10(a) plots instantaneous pressure profiles over the footprint adopting Model 2B. Numbers marking each profile refer to time. Soon after impact ($t = 2$ μs) the profile is almost uniform, similar to 1-D propagation. With time, the average pressure drops and the pressure near the perimeter of the footprint rises. There, higher pressure is needed to produce the same displacement as that at the center since it has to deform more material. This is evidenced by comparing snap-shots from Models 2A and 2B near the perimeter (compare Figs. 1(d–f) with Figs. 9(a–c)).

Fig. 10(b) plots the static pressure profile for a prescribed constant displacement over the footprint. As with the dynamic case, pressure rises steeply near the perimeter. The circles in

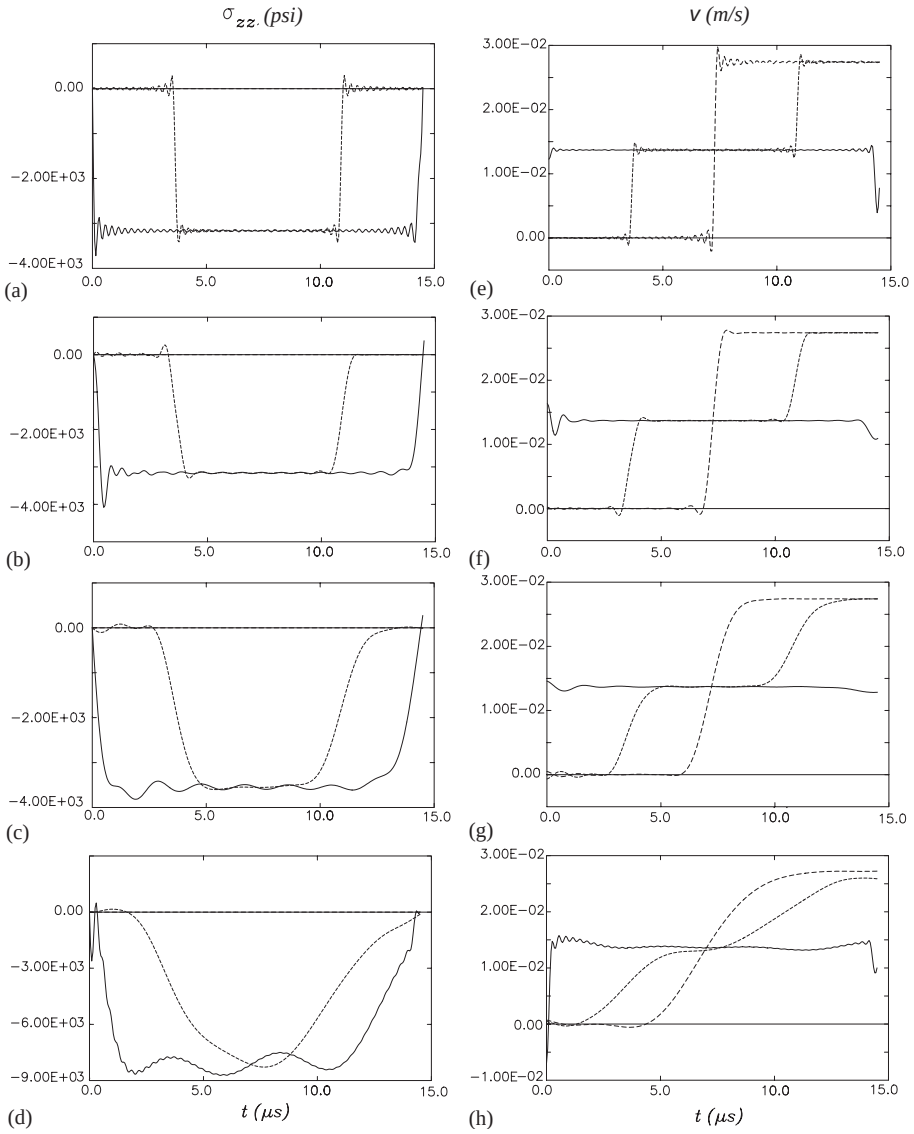

Fig. 7. Histories of stress σ_{zz} and velocity v following impact on a viscoelastic layer from the 1-D Model: (a), (e) $\tau_\sigma = 0$; (b), (f) $\tau_\sigma = 10^{-8}$ s^{-1}; (c), (g) $\tau_\sigma = 10^{-7}$ s^{-1}; (d), (h) $\tau_\sigma = 5 \times 10^{-7}$ s^{-1}; ——, $z/h = 0$; - - - - - - -, $z/h = 0.5$; – – –, $z/h = 1$.

Fig. 10(b) correspond to segment pressures p_k, and the curve corresponds to the computed normal stress σ_{zz}. All circles should lie on the curve. The offset near the perimeter is caused by truncation of the series solution in the static analysis. Both static and dynamic profiles include a periodic undulation which is an artifact caused by the finite number of pressure segments p_k in the calculation of W_{km} in Eq. (8). In the present example, the footprint radius is divided into eight segments, which explains the eight peaks on the profile.

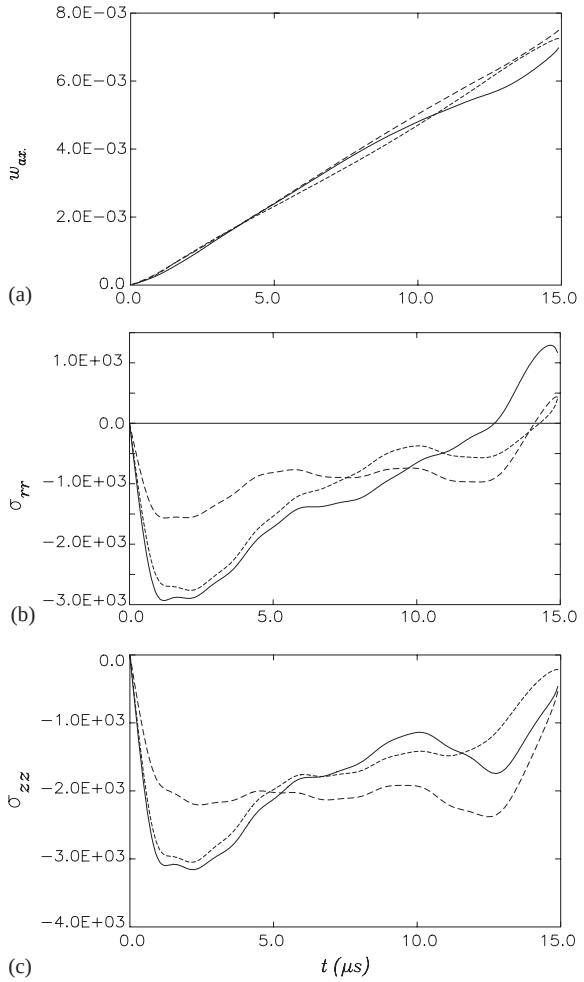

Fig. 8. Histories from 3-D axisymmetric Model 2B with prescribed velocity: (a) w, (b) σ_{rr}, (c) σ_{zz} at $z/h = 0.06$; ——, $r/r_p = 0$; - - - - -, $r/r_p = 0.5$; – – –, $r/r_p = 1$.

5. Conclusion

The transient response from impact on a weak viscoelastic disk is analyzed by four different models:

1. A 3-D axisymmetric finite volume model that couples projectile and disk.

2-A. A 3-D axisymmetric analytical model forced by prescribed pressure determined by averaging footprint pressure in Model 1.

3. A 2-D analytical model including a viscoelastic constitutive model forced as in Model 2A.

2-B. A 3-D axisymmetric analytical model forced by prescribed velocity from a 1-D model that couples projectile and disk when their radii approach infinity.

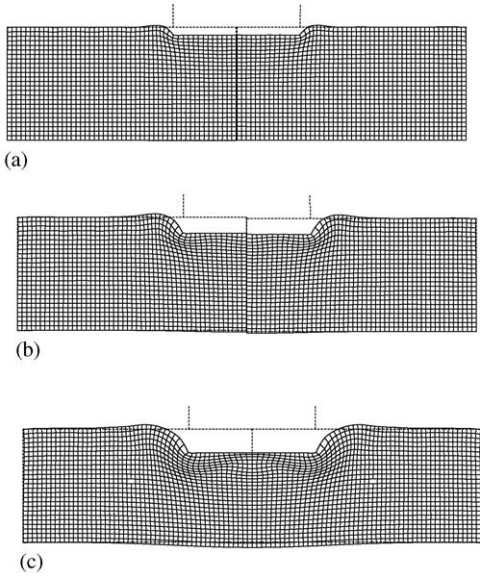

Fig. 9. Snap-shots from 3-D axisymmetric Model 2B with velocity excitation: (a) $t = 4$ μs, (b) $t = 8$ μs, (c) $t = 12$ μs.

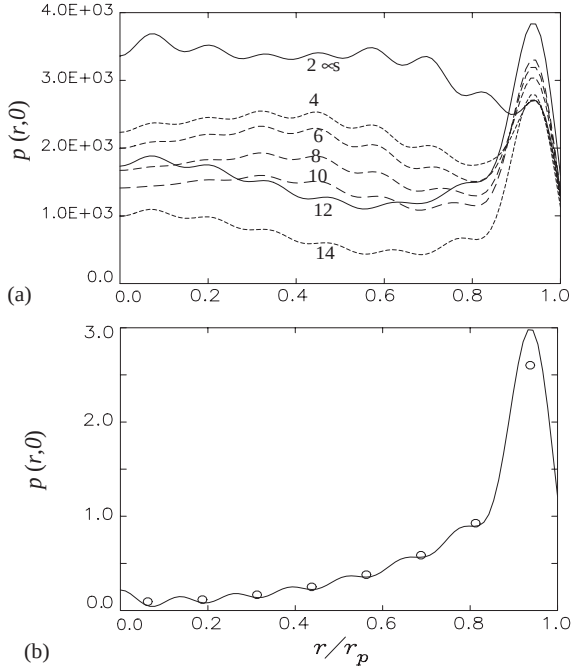

Fig. 10. Pressure distribution over foot-print from 3-D axisymmetric Model 2B with velocity excitation: (a) dynamic, (b) static.

The study revealed numerical artifacts arising from the finite volume method, the ability to relate the two different 3-D axisymmetric models via a matrix of influence coefficients, and the agreement between results predicted by the 3-D and 2-D models. More specific results follow

(1) Close to the disk axis, histories from Models 1 and 2A are similar in shape but differ in magnitude by 25%. This difference is smaller remote from impact when $r/r_p > 1$.
(2) Histories from Models 2A and 3 agree in magnitude and shape implying that the response is independent of dimensionality.
(3) In a coupled 1-D Model including viscoelasticity, the rise time increases with τ_σ because high frequency modes are filtered. The stress plateau increases with τ_σ when the transition frequency accompanied by a higher modulus falls within the frequency spectrum. Velocity is almost constant independent of τ_σ.
(4) The influence method allowing a prescribed velocity at the boundary combined with the coupled 1-D model in (3) above produce an approximate method to the fully coupled Model 1, valid when the disk material is substantially weaker than the projectile material.
(5) Histories of displacement and stress from Model 2B are closer to those from Model 1 implying that the response is sensitive to spatial distribution of applied pressure.
(6) In Model 2B, the pressure profile is almost uniform over the footprint but rises steeply to a peak near the perimeter.

Appendix A. 1-D impact of two layers including viscoelasticity

Assume that layer 1 strikes layer 2 at an initial velocity V_0. Layer 2 is initially at rest with its other face either stress free or restrained from motion. For each layer with modulus, density and thickness (E_j, ρ_j, h_j), $j = 1, 2$, the governing 1-D wave equation is

$$\frac{\partial^2 w_j}{\partial z^2} - \frac{1}{c_j^2}\frac{\partial^2 w_j}{\partial t^2} = 0, \tag{A.1}$$

where z is the co-ordinate along the thickness with origin at one face of the layer, w is displacement along z and t is time. The linear problem in (A.1) is solved by modal analysis. Let

$$w_j(z,t) = w_{0j}(z)\mathrm{e}^{\mathrm{i}\omega t}, \quad \mathrm{i} = \sqrt{-1}, \tag{A.2}$$

where $w_{0j}(z)$ are functions of z only and ω is frequency in radians per second. Substituting Eq. (A.2) in (A.1) yields a solution in the form

$$w_{0_j}(z) = A_j \sin(k_j z) + B_j \cos(k_j z), \quad k_j = \omega/c_j. \tag{A.3}$$

The striking layer 1 is stress free at $z = 0$ while the struck layer 2 can either be stress free or restrained from motion over its other face:

$$\sigma_{01}(0) = 0; \quad \sigma_{02}(h_2) = 0, \quad \text{stress-free}; \quad \text{or} \quad u_{02}(h_2) = 0, \quad \text{restrained}. \tag{A.4}$$

At the interface of the two layers, displacement and stress are continuous

$$u_{01}(h_1) = u_{02}(0), \quad \sigma_{01}(h_1) = \sigma_{02}(0). \tag{A.5}$$

Invoking the constitutive law and enforcing Eqs. (A.4) and (A.5) produces

$$\begin{aligned} &A_1 = 0, \quad A_2 = -B_2 \cot(k_2 h_2) \quad \text{or} \quad A_2 = B_2 \tan(k_2 h_2), \\ &B_1 \cos(k_1 h_1) = B_2, \\ &-E_1 k_1 B_1 \sin(k_1 h_1) = \begin{cases} E_2 k_2 B_2 \tan(k_2 h_2), & \text{stress-free}, \\ -E_2 k_2 B_2 \cot(k_2 h_2), & \text{restrained}, \end{cases} \end{aligned} \tag{A.6}$$

for each of the two conditions on face 2 of layer 2. The last two equations in Eq. (A.6) yield the dispersion relations

$$\begin{aligned} &\rho_1 c_1 \sin(k_1 h_1) \cos(k_2 h_2) + \rho_2 c_2 \cos(k_1 h_1) \sin(k_2 h_2) = 0, \quad \text{stress-free}, \\ &\rho_1 c_1 \sin(k_1 h_1) \sin(k_2 h_2) - \rho_2 c_2 \cos(k_1 h_1) \cos(k_2 h_2) = 0, \quad \text{restrained}, \end{aligned} \tag{A.7}$$

which determine resonant states and corresponding modal state vectors

$$\begin{aligned} &w_{01}(z) = \cos(k_1 z), \quad \sigma_{01}(z) = -\omega \rho_1 c_1 \sin(k_1 z), \\ &w_{02}(z) = \begin{cases} \dfrac{\cos(k_1 h_1)}{\cos(k_2 h_2)} \cos(k_2(h_2 - z)), & \text{stress-free}, \\ \dfrac{\cos(k_1 h_1)}{\sin(k_2 h_2)} \sin(k_2(h_2 - z)), & \text{restrained}, \end{cases} \\ &\sigma_{02}(z) = \begin{cases} \omega \rho_2 c_2 \dfrac{\cos(k_1 h_1)}{\cos(k_2 h_2)} \sin(k_2(h_2 - z)), & \text{stress-free}, \\ -\omega \rho_2 c_2 \dfrac{\cos(k_1 h_1)}{\sin(k_2 h_2)} \cos(k_2(h_2 - z)), & \text{restrained}. \end{cases} \end{aligned} \tag{A.8}$$

The modal solution proceeds by expanding w_j in terms of the eigenfunctions

$$w_j(z, t) = \sum_{k=1}^{M} a_k(t) w_{jk}(z). \tag{A.9}$$

Substituting Eq. (A.9) in Eq. (A.1) and enforcing orthogonality of the $w_{0j}(x)$ set yields

$$(\ddot{a}_k(t) + \omega_k^2 a_k(t)) N_k = 0, \tag{A.10}$$

where ω_k are solutions of the dispersion relations (A.7) and N_k is generalized mass given by

$$\begin{aligned} N_k &= \sum_{j=1}^{2} \rho_j \int_0^{h_j} w_{0j}^2(z)\, \mathrm{d}z \\ &= \begin{cases} \dfrac{\rho_1 h_1}{2}\left(1 + \dfrac{\sin(2k_1 h_1)}{2k_1 h_1}\right) + \dfrac{\rho_2 h_2}{2}\left(1 + \dfrac{\sin(2k_2 h_2)}{2k_2 h_2}\right)\dfrac{\cos^2(k_1 h_1)}{\cos^2(k_2 h_2)}, & \text{stress-free}, \\ \dfrac{\rho_1 h_1}{2}\left(1 + \dfrac{\sin(2k_1 h_1)}{2k_1 h_1}\right) + \dfrac{\rho_2 h_2}{2}\left(1 - \dfrac{\sin(2k_2 h_2)}{2k_2 h_2}\right)\dfrac{\cos^2(k_1 h_1)}{\sin^2(k_2 h_2)}, & \text{restrained}. \end{cases} \end{aligned} \tag{A.11}$$

The initial conditions are

$$\dot{w}_1(z,0) = V_0, \quad w_1(z,0) = 0, \quad \dot{w}_2(z,0) = 0, \quad w_2(z,0) = 0. \tag{A.12}$$

Substituting Eq. (A.12) in Eq. (A.10) and enforcing orthogonality of $w_{0j}(x)$ yields

$$a_k(0) = 0, \quad \dot{a}_k(0) = \frac{V_0\rho_1}{N_k}\int_0^{h_1} w_{01}(z)\,\mathrm{d}z = \frac{V_0\rho_1 c_1}{N_k\omega_k}\sin(k_{1k}h_1). \tag{A.13}$$

The solution of Eq. (A.10) subject to the initial conditions (A.12) produces

$$\begin{aligned} &a_k(t) = C_{1k}\cos(\omega_k t) + C_{2k}\sin(\omega_k t),\\ &C_{1k} = 0, \quad C_{2k} = \frac{\dot{a}_k(0)}{\omega_k} \equiv \frac{V_0\rho_1 c_1}{N_k\omega_k^2}\sin(k_{1k}h_1). \end{aligned} \tag{A.14}$$

Expressions of the state vector take the form

$$w_j(z,t) = \sum_{k=1}^{M} C_{2k}\sin(\omega_k t)w_{0jk}(z), \quad \sigma_j(z,t) = \sum_{k=1}^{M} C_{2k}\sin(\omega_k t)\sigma_{0jk}(z), \tag{A.15}$$

where C_{2k} is given by Eq. (A.14) and the modal state vector $\{w_{0jk}, \sigma_{0jk}\}$ is given by Eq. (A.8).

The simplest constitutive law of a linear viscoelastic solid includes stress, strain and their first derivatives in time:

$$\sigma + \tau_\varepsilon\frac{\partial\sigma}{\partial t} = E_o\left(\varepsilon + \tau_\sigma\frac{\partial\varepsilon}{\partial t}\right), \tag{A.16}$$

where $\tau_\sigma, \tau_\varepsilon$ are relaxation and creep time constants and E_o is a modulus [17]. This model is termed $V_e(1,1)$ to indicate that it includes time derivatives in stress and strain up to the first. In the frequency domain Eq. (A.16) yields

$$\sigma = E_o\frac{(1+\tau_\sigma \mathrm{i}\omega)}{(1+\tau_\varepsilon \mathrm{i}\omega)}\varepsilon. \tag{A.17}$$

Eq. (A.17) defines the complex modulus

$$E_c = \frac{(1+\tau_\sigma \mathrm{i}\omega)}{(1+\tau_\varepsilon \mathrm{i}\omega)}E_o \tag{A.18}$$

and the loss coefficient η is defined by

$$\eta = (E_c)_{im}/|E_c| \equiv \frac{\omega(\tau_\sigma - \tau_\varepsilon)}{1+\omega^2(\tau_\sigma\tau_\varepsilon)}; \tag{A.19}$$

η_{max} is reached when ω_T satisfies

$$\omega_T\sqrt{\tau_\sigma\tau_\varepsilon} = 1 \Rightarrow \eta_{max} = \omega_T(\tau_\sigma - \tau_\varepsilon)/2. \tag{A.20}$$

In the limits of zero or infinite strain-rate the modulus asymptotes to the rubbery modulus E_R, or the glassy modulus E_G, respectively. Applying these limits to Eq. (A.18) produces

$$E_R = E_o, \quad E_G = E_o\tau_\sigma/\tau_\varepsilon. \tag{A.21}$$

Eqs. (A.18)–(A.21) determine $\tau_\sigma, \tau_\varepsilon$ uniquely provided E_R, E_G and ω_T are known.

The complex modulus defined in Eq. (A.18) changes c_j and k_j in Eq. (A.3) into complex quantities. These in turn convert (A.7) into an implicit complex eigenvalue problem with eigenvalues

$$\omega_j = \omega_{Rj} + \mathrm{i}\omega_{Ij}, \quad \omega_{Rj} > 0, \ \ \omega_{Ij} > 0. \tag{A.22}$$

Unlike the purely elastic case which admits the eigenvalue pair $\pm\omega_j$ for each eigenfunction, in the viscoelastic case this pair is $+\omega_j$ and $-\omega_j^*$ (not $-\omega_j$) where $(\,)^*$ stands for complex conjugate. This means that $\omega_{1j} = \omega_{Rj} + \mathrm{i}\omega_{Ij}$ and $\omega_{2j} = -\omega_{Rj} + \mathrm{i}\omega_{Ij}$. The reason ω_I retains the same sign for both solutions is that ω_I is a measure of damping which reduces amplitude whether the real frequency is $+\omega_{Rj}$ or $-\omega_{Rj}$. Consequently the equation governing $a_j(t)$ in Eq. (A.10) becomes

$$\left(\frac{\mathrm{d}}{\mathrm{d}t} - \mathrm{i}\omega_j\right)\left(\frac{\mathrm{d}}{\mathrm{d}t} + \mathrm{i}\omega_j^*\right)a_j(t) = 0$$

$$\Rightarrow \left[\frac{\mathrm{d}^2}{\mathrm{d}t^2} + \mathrm{i}(\omega_j^* - \omega_j)\frac{\mathrm{d}}{\mathrm{d}t} + \omega_j\omega_j^*\right]a_j(t) = 0. \tag{A.23a}$$

Noting that $\mathrm{i}(\omega_j^* - \omega_j) = 2\omega_{Ij}$ and $\omega_j\omega_j^* = \omega_{Rj}^2 + \omega_{Ij}^2$, Eq. (A.23a) simplifies to

$$\left[\frac{\mathrm{d}^2}{\mathrm{d}t^2} + 2\omega_{Ij}\frac{\mathrm{d}}{\mathrm{d}t} + \omega_{Rj}^2 + \omega_{Ij}^2\right]a_j(t) = 0. \tag{A.23b}$$

Clearly, ω_{Ij} acts as a velocity proportional viscous damper. Rewriting Eq. (A.23b) in standard form:

$$\left[\frac{\mathrm{d}^2}{\mathrm{d}t^2} + 2\zeta_j\bar{\omega}_j\frac{\mathrm{d}}{\mathrm{d}t} + \bar{\omega}_j^2\right]a_j(t) = 0, \quad \zeta_j = \frac{\omega_{Ij}}{\bar{\omega}_j}, \quad \bar{\omega}_j = \sqrt{\omega_{Rj}^2 + \omega_{Ij}^2}. \tag{A.24}$$

References

[1] M.L. Wilkins, The use of artificial viscosity in multidimensional fluid dynamics calculations, University of California, Lawrence Livermore National Laboratory, Rept. UCRL-78348, 1976.

[2] J.O. Hallquist, A procedure for the solution of finite deformation contact–impact problems by the finite element method, University of California, Lawrence Livermore National Laboratory, Rept. UCRL-52066, 1976.

[3] J.O. Hallquist, DYNA2D—an explicit finite element and finite difference code for axisymmetric and plane strain calculations (User's Guide), University of California, Lawrence Livermore National Laboratory, Report UCRL-52429, March, 1978.

[4] G.L. Goudreau, J.O. Hallquist, Recent developments in large scale finite element Lagrangian hydrocode technology, *Computer Methods in Applied Mechanics and Engineering* 33 (1982) 725–757.

[5] J.J. Monaghan, Shock simulation by the particle method SPH, *Journal of Computational Physics* 52 (1983) 374–389.

[6] B. Nayroles, G. Touzot, P. Villon, Generalizing the finite element method: diffuse approximation and diffuse elements, *Computational Mechanics* 10 (1983) 307–318.

[7] F.P. Stecher, G.R. Johnson, Lagrangian computations for projectile penetration into thick plates, in: W.A. Grover (Ed.), *Computers in Engineering*, vol. 2, ASME, New York, 1984, pp. 292–299.

[8] R.B. Haber, A mixed Eulerian–Lagrangian displacement model for large-deformation analysis in solid mechanics, *Computer Methods in Applied Mechanics and Engineering* 43 (1984) 277–292.

[9] W.K. Liu, T. Belytschko, H. Chang, An arbitrary Lagrangian–Eulerian finite element method for path-dependent materials, *Computer Methods in Applied Mechanics and Engineering* 58 (1986) 227–245.

[10] D.J. Bammann, Modeling temperature and strain rate dependent large deformation of metals, *Applied Mechanics Reviews* 43 (1990) 312–319.
[11] S. Ghosh, N. Kikuchi, An arbitrary Lagrangian–Eulerian finite element method for large deformation analysis of elastic-viscoplastic solids, *Computer Methods in Applied Mechanics and Engineering* 86 (1991) 127–188.
[12] L.D. Libersky, A.G. Petschek, T.C. Carney, J.R. Hipp, F.A. Allahdadi, High strain Lagrangian hydrodynamics, *Journal of Computational Physics* 109 (1995) 67–75.
[13] T. Belytschko, Y.Y. Lu, L. Gu, Element-free Galerkin methods, *International Journal of Numerical Methods in Engineering* 37 (1994) 229–256.
[14] M. El-Raheb, P. Wagner, Wave propagation in a plate after impact by a projectile, *Journal of the Acoustical Society of America* 82 (1987) 498–505.
[15] M. El-Raheb, P. Wagner, Transient elastic waves in finite layered media: three-dimensional axisymmetric analysis, *Journal of the Acoustical Society of America* 99 (1996) 3513–3527.
[16] M. El-Raheb, Dynamics of a 2-D composite of elastic and visco-elastic layers, *Journal of the Acoustical Society of America* 112 (2002) 1445–1455.
[17] Y.C. Fung, *Foundations of Solid Mechanics*, 1st Edition, Prentice-Hall, Englewood Cliffs, NJ, 1965, pp. 22–27.